On the spreading of high-pressure spray-generated liquid wall films

Quentin Lamiel, Nicolas Lamarque, Jerome Hélie, Dominique Legendre

Version of Record: https://www.sciencedirect.com/science/article/pii/S0301932221000677
Manuscript_a429cb8a191886c5cd497fc52208e34a

On the Spreading of High-Pressure Spray-Generated Liquid Wall Films

Quentin Lamiel[a,b], Nicolas Lamarque[b], Jerome Hélie[b], Dominique Legendre[a]

[a]*Institut de Mécanique des Fluides de Toulouse (IMFT) - Université de Toulouse, CNRS-INPT-UPS, Toulouse, France*
[b]*CPT France SAS, 1 avenue Paul Ourliac BP 1149, 31036 Toulouse, France*

Abstract

The spreading of a n-decane liquid film induced by the impingement of a spray generated by a high-pressure injector is studied experimentally. The experimental setup uses the Refractive Index Matching (RIM) method to observe the development and propagation of the wall film. The influence of injection time, injection pressure, temperature, and injector to wall distance are considered. The film evolution on the wall presents two clear distinct phases. During the injection phase the film area is growing linearly with respect to time. Once the injection is stopped, the film relaxes to its maximal expansion. Each phase is accurately described using a simple modeling based on mass and momentum balance in the liquid film.

Keywords: Film spreading, High-pressure sprays wall impingement, refractive index matching method

1. Introduction

High-pressure sprays are encountered in many industrial processes such as in steel industry (Chen and Tseng, 1992), in painting (Garbero et al., 2002), irrigation (Stevenin et al., 2016), and as well as in automotive engines (either for gasoline or diesel injection) (Moreira et al., 2010). The injection process has been identified as a key factor in the generation of pollutants like the particulate matter (Ashgriz, 2011) and the formation of liquid films on both the chamber wall and the piston is suspected to be a significant source of pollution (Leach et al., 2018). Many different technologies are used to make high-pressure injectors, producing very different sprays (Lefebvre, 1988). A spray is composed by millions of droplets, with various sizes and velocities. It also has some geometrical characteristics, such as its cone angle or its penetration (Naber and Siebers, 1996), whether it is plain or hollow. These macroscopic and microscopic characteristics have been carefully studied both experimentally (Wigley et al., 1999) and numerically (Hélie et al., 2016). For instance Phase Doppler Anemometry method (PDA) (Takeda, 2006; Kalantari and Tropea, 2007; Araneo and Tropea, 2000) gives the size and velocity repartition of droplets through time. The geometrical characteristics of high-pressure sprays can be obtained using imaging techniques like, for example, shadowgraphy, Mie scattering or Schlieren techniques (Naber and Siebers, 1996; Mojtabi et al., 2014; Parrish, 2014; Krämer et al., 2014; Montanaro et al., 2016).

The objective of this study is to focus on the spreading of a liquid film generated by a high pressure injector. Fluid spreading after deposition on a wall has been extensively considered for two cases: a single droplet impacting a surface (Josserand and Thoroddsen, 2016) and a droplet deposited on a wall (Bonn et al., 2009a). Depending on the nature of the effects in competition, different spreading rates have been reported. The objective is here to consider the spreading when generated by a high pressure spray. For that purpose, an experimental set-up has been developed to follow the film evolution and spreading during and after the injection process. The paper is organized as follows. We first describe the experimental setup and the Refractive Index Matching (RIM). The results are then described and the different phases of the spreading are depicted and modeled.

2. Experimental set-up

The experimental set-up presented in Figure 1 is composed of a fuel preparation system, a multi-hole injector, an impingement plate and a camera. The fuel preparation system consists in a low-pressure pump supplied by a 12V DC generator and it feeds a high-pressure pump run by an electric motor. Fuel pressure P_i can be varied from 15 to 250 bar and specially designed flexible hoses are used to transport the fuel from the pump to the injector. Three injection pressures are considered here: 50, 100 and 200 bars. The injector is a three-hole solenoid GDI research injector developed by Continental Automotive. The three holes produce full cone sprays and only one of them is directed towards the impingement plate whereas the two others are venting away and do not contribute to the film. They also have the same geometrical characteristics with equally distributed mass flow rate resulting in mass flow rates per hole $\dot{m} = 1.53, 2.17, 3.06\ g/s$, corresponding to flow rates $Q = 2.27, 3.21, 4.54$ cm^3/s at $P_i = 50, 100, 200$ bar, respectively, following an evolution of the form $Q \propto \sqrt{P_i}$ characteristic of this type of injector (Mohan et al., 2018). The main spray characteristics such as the droplets size distribution and spray expansion are depicted in the Appendix. The duration of injection T_i is also a parameter of control and it has been varied from 2 to 12 ms (note it is rarely more than around 5ms for combustion applications). The injector is located at a distance z to the substrate. z has been varied from 20 mm to 65 mm which is typical of current GDI engines. It is piloted by a Continental Solenoid driver box (ECU). The trigger signals are generated by a National Instrument card, driven by a home-made LabView software.

All the results presented in this study are obtained with n-decane (fuel), which is not really common for studies involving GDI injectors. The choice of n-decane has been motivated by several reasons. It is representative enough of gasoline in term of viscosity and density, and it is less volatile than n-heptane. It then allows a greater range of temperature variation and is more satisfying for safety reasons. Two temperatures of injection are considered $T_{FU} = 20°$C (room temperature) and $T_{FU} = 90°$C (the maximum temperature allowed in our lab for safety reasons). Most of the experiments have been conducted for $T_{FU} = 90°$C. By heating the plate to $T_W = 90°$C all the tiny droplets that deposit on the sapphire further from the liquid film edge vaporize. It improves the visualisation of the film front and makes easier the image post-treatment. The corresponding values of the density, viscosity and surface tension are $\rho = 729$ kg/m^3, $\eta = 8.86\,10^{-4}$ Pa.s, $\gamma = 23.8$ mN/m for $T_{FU} = 20°$C and $\rho = 676$ kg/m^3, $\eta = 3.99\,10^{-4}$ Pa.s, $\gamma = 17.4$ mN/m for $T_{FU} = 90°$C.

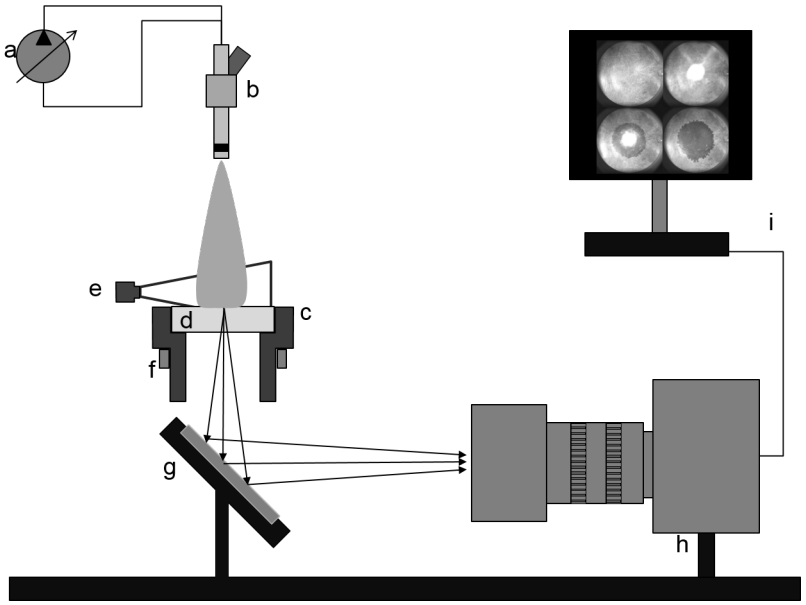

Figure 1: Sketch of the Refractive Index Matching experimental setup. a) High-pressure pump, b) GDI injector, c) Plate holder, d) Impinging plate, e) Light source, f) Heating collar, g) Mirror, h) High-Speed Video camera, i) Computer.

The impingement plate is a 5mm-thick circular sanded sapphire window (Kircheim optics) with a 60mm diameter. A characterization of the surface has been performed with an Atomic Force Microscope (AFM). The measure based on 15 different samples of $100 \times 5\mu\text{m}^2$ gives an arithmetical mean deviation for the surface profile of 0.43 μm. The wetting property of the sapphire plate has been characterized using a goniometer. The value of the advancing and receding contact angles for the n-decane were found to be $\theta_a = 11 \pm 2°$ and $\theta_r = 3 \pm 2°$, respectively.

A circular aluminum holder has been designed to allow visualization from the bottom of the plate. It also allows one to fix a heating collar and, hence, heats the plate up to 250°C. The heating system is therefore composed of a thermocouple, fixed on the element to heat, a PID controller and a heating collar. The accuracy of the system is 0.5°C and both the temperature injector T_{FU} and the temperature of the impingement plate T_W can be heated independently at a specific temperature. This study has been conducted for equal temperatures $T_W = T_{FU}$ and a room temperature of 20^{o}C.

A fixation rail allows to support the plate holder and, in the same plan, a holder for a mirror. The mirror is tilted at 45° to redirect the light to the camera. The High-Speed Videocamera is a Phantom V1210 with a CMOS sensor. The sample rate used is 20 kHz, with an exposition time of 10 μs. It is connected to a 60mm Nikon objective.

The objective of the study is to consider the spreading of a liquid film generated by a high pressurized spray impacting a wall. Such a spray is classically composed of tiny droplets of characteristic size of order 10 to 20 μm. Typical shadowgraph images of sprays are shown in Figure 2 and the corresponding spray characteristics are depicted in Appendix. Instantaneous images reveals a classical jet dynamics with the development of unsteadiness patterns that capture droplets at the jet periphery (Hélie et al., 2016). The average image, performed once the liquid has

reached the edges of the field of view, gives a clear view of the jet expansion. The jet expansion is larger close to the injector tip. Then, once the surrounding air is entrained enough, the spray expansion gets smaller and the angle of the jet cone is observed to range from $8 - 15°$ (Ghosh and Hunt, 1994; Hélie et al., 2016). When impacting the wall, the spray both generates a liquid film and a secondary spray (Ko and Arai, 2002). These points and their consequences on the film propagation will be further analyzed and integrated in the modeling proposed to describe the film expansion.

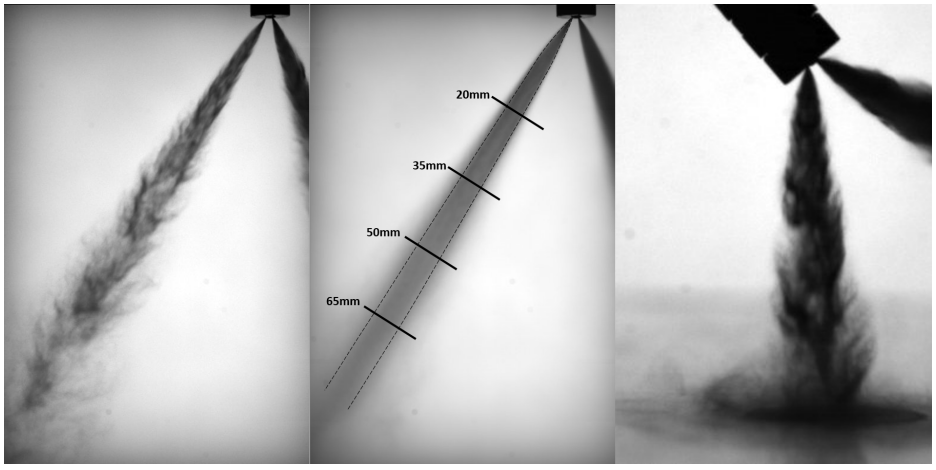

Figure 2: Spray shadowgraphy for injection pressure $P_i = 100$bars. (left) Instantaneous image showing the jet structure development without the impacting plate. The corresponding video is given in the supplementary material. (center) View of the mean jet expansion without the impacting plate. The lines represent the distances z=20, 35, 50 and 65 mm to the injector. (right) Spray impinging upon the plate and the two other sprays (almost superimposed) are venting away.

2.1. The RIM method

The RIM method detailed in Figure 3 has been used to measure the film spreading. The Rim method makes possible a direct non-invasive observation of liquid films (Yang and Ghandhi, 2007; Maligne and Bruneaux, 2011; Lamiel et al., 2017). A rough transparent plate is illuminated at a grazing angle by a fiber optic light guide connected to a LED spot. As liquid is filling the troughs on the impingement plate surface, the light ray paths are changed and the wetted surface transmits less light than the dry surface (Figure 3) requiring very close refractive index for the substrate and the liquid. Light is collected from below by a mirror that redirects it to the camera (Figure 1). After a fine calibration of the measure, the grey level can be linked to the thickness of the liquid film (Drake et al., 2003; Maligne and Bruneaux, 2011). This method has some limits, especially when the observation is performed during the injection process. Indeed, both mie scattering induced by the droplets forming the spray (Figure 4) and waves propagating on the film (see section 3.1) make an accurate thickness measurement impossible in our system.

Because of these restrictions, the RIM method is used in this study to accurately determine the film spreading and just a clear detection of the film front is required. For that purpose, a smooth sapphire plate is used. The plate has been sanded on one face, so that the roughness level (less

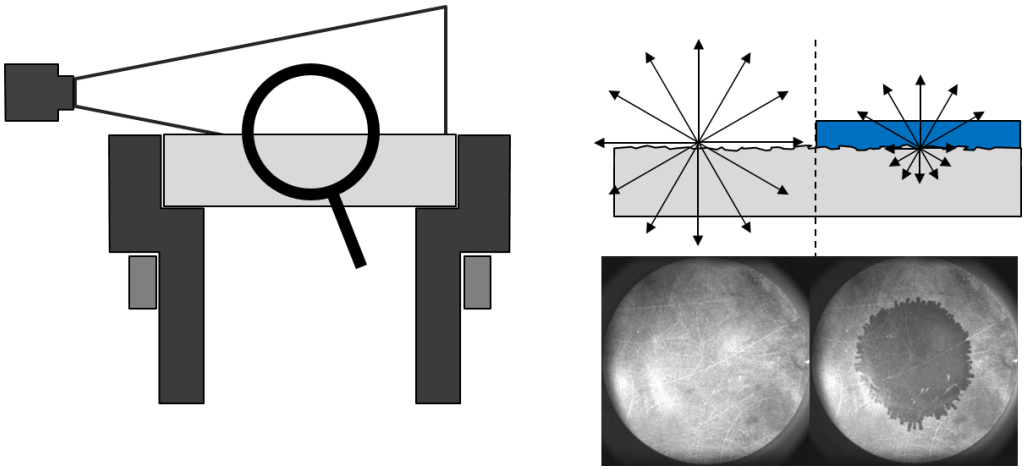

Figure 3: Principle of RIM measurement. Left: Grazing Light illuminating a transparent plate; Right: Modification of light path caused by wetting making a clear detection of the wetted surface.

than 1 μm) is negligible compared to the thickness of the liquid film that we will see later to be of order $10 - 20$ μm. However the surface is rough enough to perform a clear visualization of the wetted surface so that the surface is dark when the sapphire is wet (Figure 3, Right), the refractive index of the sapphire and the decane being close enough ($n_{\text{Decane}} = 1.41$ and $n_{\text{Sapphire}} = 1.77$). It makes possible a binary description of the surface, either dry or wet, and the film is then clearly determined as shown in the figure. It also has the great interest to make the wetted area detection not sensible to the waves that propagates on the film. However, the spray droplets between the injector and the plate are scattering the light coming from the optical fibre and are responsible of the white area observed at the center of the liquid film as observed in Figure 4. As a consequence, it makes the liquid film difficult to observe at the early stages of injection (until around 1ms after the start of impingement). Once the liquid film has spread enough, it is possible to track its edge (dark area) in order to get the area of the liquid film. In the following, the film area is reported after $t = 1ms$.

3. Results

3.1. Film spreading description

An example of film spreading is depicted in Figure 4 for an injection time $T_i = 6$ms, a fuel pressure $P_i = 100$ bar and a distance $z = 50\,\text{mm}$. Two different injection temperatures, $T_{FU} = 20^o$C (room temperature) and $T_{FU} = 90^o$C, are reported. As observed, the contrast on the images is better at 90^oC making much easier the film detection and the image processing. Indeed, at this temperature, tiny droplets deposing further than the edges of the liquid film and perturbing the contour detection are quickly vaporized. As observed, the film area is almost circular during all the spreading process.

Using the software Fiji (Schindelin et al., 2012) and several image processing tools, it is possible to track the liquid film edge and, hence, determine the time evolution of the film surface area. Figure 5 compares the area evolution of the liquid film corresponding to the images reported in

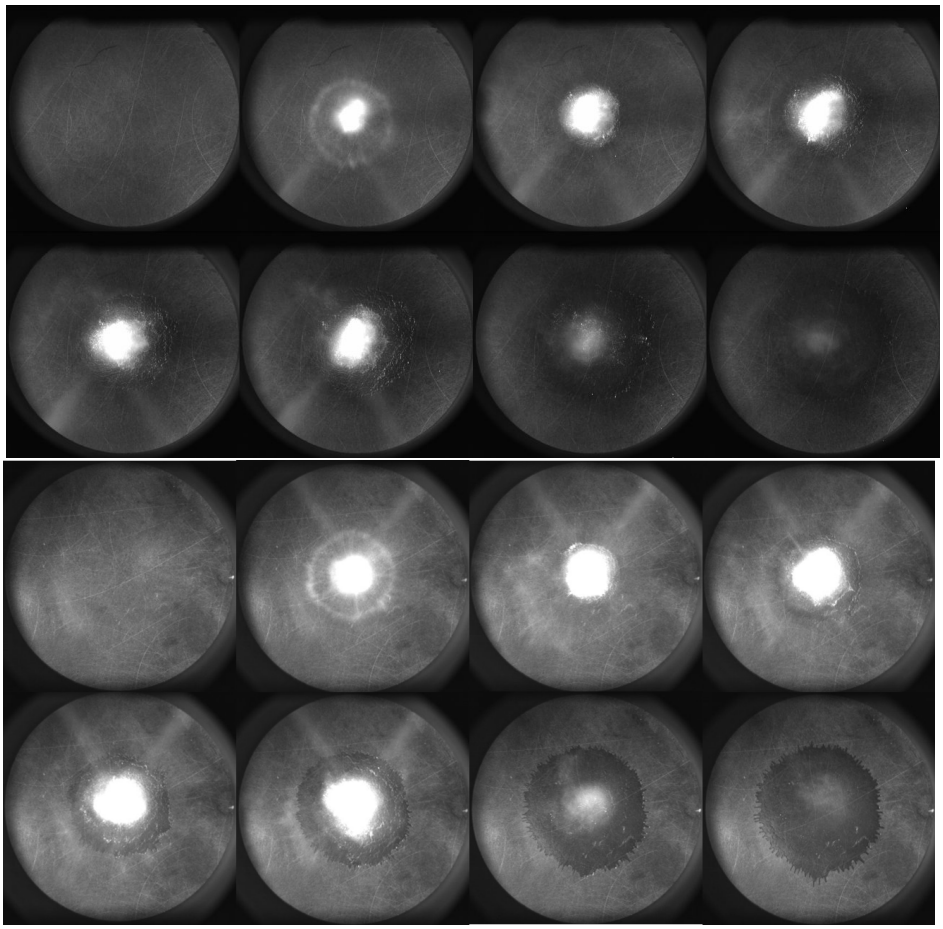

Figure 4: Images of a film spreading as visualized from bottom on the RIM setup. $P_i = 100\,\mathrm{bar}$ $T_i = 6\,\mathrm{ms}$ and $z = 50\,\mathrm{mm}$. (top) $T_{FU} = T_W = 20^oC$, bottom $T_{FU} = T_W = 90^oC$. Images are displayed every $1.25\,\mathrm{ms}$. The corresponding video is given in the supplementary material.

Figure 4 for the two injection temperatures. It displays the average of 5 repetitions, together with error bars, which represent the typical standard deviation observed in our experiments. This shows the good repeatability of the injection, the spray wall impingement and the film spreading. In what follows, error bars will not be displayed for the sake of clarity.

A similar evolution is observed for the two temperatures. During the early stage of injection, the first droplets are piling up to create a liquid film. As explained, the contour of this liquid film is difficult to identify because of a strong Mie scattering from the spray and the first measurement point is taken 1ms after the impact of the first droplets on the plate. This value of 1 ms is the time necessary to be able to detect the liquid film spreading outside the impingement area A_0 corresponding to an initial detected radius R_0 for the liquid film. Once the liquid film is created, it is spreading and the edge of the film can be tracked. As shown in Fig. 5, the spreading can be separated into two main phases: the film spreading observed during the injection and a relaxation phase following the closing of the injector needle. As the impingement is orthogonal to the plate, the spreading rate is almost the same in all directions and the mean film shape is almost a circle.

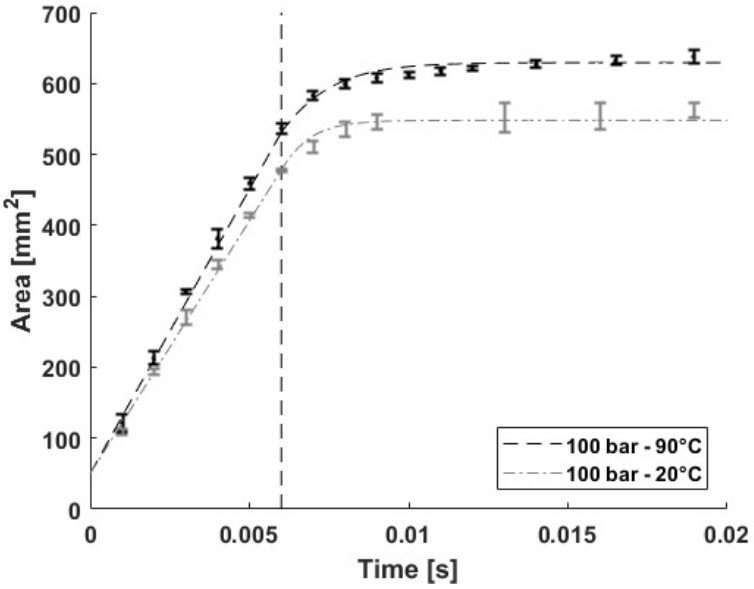

Figure 5: Time evolution of the liquid film area for $T_{FU} = T_W = 20^o$C (grey line) and $T_{FU} = T_W = 90^o$C (dark line). Experimental conditions: $T_i = 6$ ms, $P_i = 100$ bar, $z = 50$ mm. The vertical dashed line indicates the end of injection. The dashed lines correspond to the corresponding modeling for both the injection phase and the relaxation phase (see description in the text).

During the spreading phase, the liquid film area is observed to grow linearly with respect to time. After the end of injection, the film dynamics changes. It still continues to slowly grow for some moments, due to its inertia. This last phase will be called the relaxation phase. For the cases reported in Fig. 5, the area stabilizes to $A \approx 550$mm^2 and $A \approx 630$mm^2 corresponding to a final radius $R \approx 12.6$mm and $R \approx 14.2$mm for $T_{FU} = 20^o$C and $T_{FU} = 90^o$C, respectively. As expected the film spreads faster at larger temperature because of a lower viscosity resulting in a larger final liquid film surface at both the end of injection and relaxation phase. This point will be discussed latter in the paper. As commented with Fig. 4 the film front detection is significantly improved when the temperature is increased. For this reason the following parametric investigation is conducted at $T_{FU} = T_W = 90^o$C.

As can be observed in Figure 4 digitations develop at the edge of the liquid film. The so called digitations look like fingers disturbing the regular shape of the liquid film edge but their size always remains much smaller than the film radius. Inserts of Figure 6 show a magnification of these digitations, for the three pressure of injection considered (50, 100, 200 bar). Increasing the injection pressure promotes the apparition of the fingers. The physical explanation of the fingers formation seems similar to the ones observed for falling film. When a thin liquid film falls down an inclined plate, a capillary ridge forms behind the advancing front. An instability appears on the front and digitations structures develop as thicker regions progress faster than thinner regions (Spaid and Homsy (1996); Bonn et al. (2009b)). The digitations wavelength has been determined as follows. After the end of injection, the number of digits on several portions of the liquid film is recorded. The number of fingers is then extended to the full liquid film front assuming

that the instability development is the same in all directions. Hence, it gives a wavelength λ that is normalized by the corresponding mean film perimeter $2\pi R$. This normalized digitation wavelength is reported in Figure 6 as a function of the injection pressure. A power law of the form $\lambda/R \propto P_i^{-1/3}$ is observed. Such behavior is consistent with the equivalent presented in Huppert (1982); Silvi and Dussan V (1985); Lavalle et al. (2020). They studied the apparition of fingers on a liquid film flowing down a plate. In this situation, the liquid driving is controlled by $\rho g \sin\alpha$ where α is the slope of the surface and the wavelength of the growing instability follows the power law $\lambda \propto (\rho g \sin\alpha)^{-1/3}$. The same power law is here observed with the pressure of injection P_i that drives the film expansion.

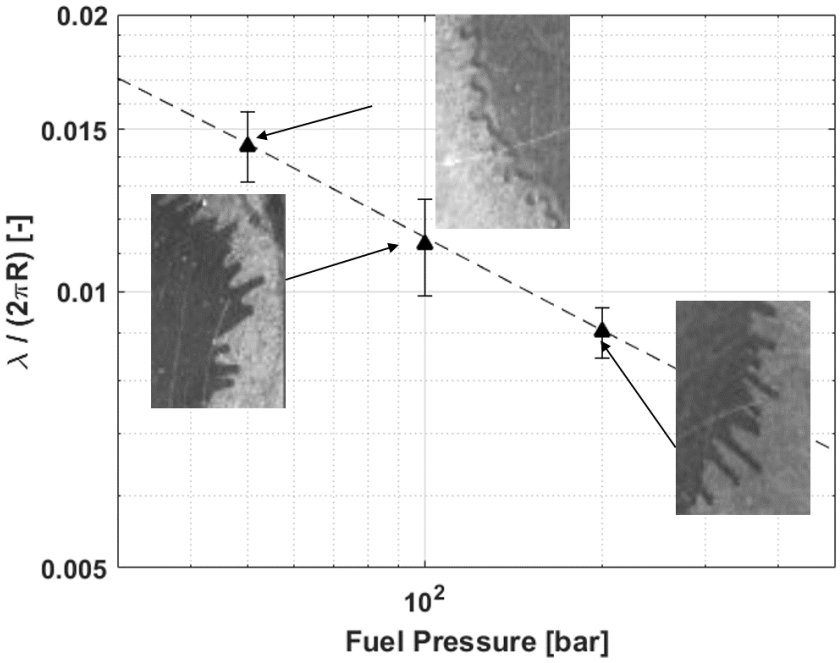

Figure 6: Evolution of digitation wavelength with respect to fuel pressure for $T_i = 6$ms and $z = 50$mm. The dashed line represent the power law $P_i^{-1/3}$. Errors bars show rms values of the measurements.

An other feature identified during the film spreading is the apparition of waves while the liquid film is propagating, as can be observed in Figure 7 for different injection conditions. High-pressure sprays are turbulent and thus a place where many micro and macroscopic motions are created (Fansler and Parrish, 2014; Heinlein and Fritsching, 2006). A well known consequence of the spray inner-motion is the so-called droplet clustering (Squires and Eaton, 1991; Fansler and Parrish, 2014). By looking carefully at the movies, it becomes quite clear that the waves are generated by the spray inhomogeneities and oscillations that impact the film surface (see Figure 2 and the corresponding video given in the supplementary material). Similar observations were recently reported by Li et al. (2019) and Xiao et al. (2020). These waves propagate at a velocity larger than the spreading velocity. For each pressure, the velocity of the waves flowing over the liquid film have been tracked for different radial positions. The relative wave velocity is obtained by

subtracting the film speed at the wave position. In Figure 7 the relative velocity of several waves
185 is displayed for $P_i = 100$ bar. The wave velocity is found in the range 1 to 15 m/s. The maximum value is observed close to the impact zone and it decays following the power law $(r - R_0)^{-1/2}$, where R_0 corresponds to the mean radius of the periphery of the impingement surface $A_0 = \pi R_0^2$. Such evolution in $r^{-1/2}$ is consistent with planar radial waves propagation (Lighthill, 2001).

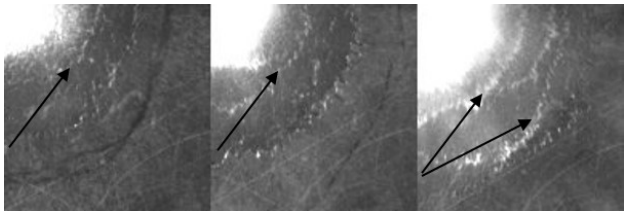

Figure 7: Detail of surface waves for different injection conditions for $T_i = 10$ ms and $z = 50$ mm. Left to Right: 50, 100, 200 bar.

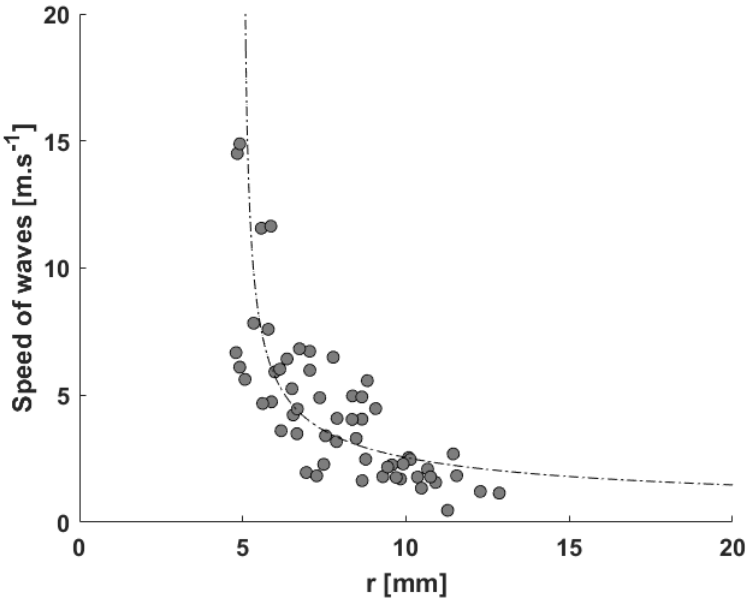

Figure 8: Evolution of film surface waves speed with respect to their radial position r. Experimental conditions $P_i = 100$ bar, $T_i = 10$ ms and $z = 50$ mm. The curves represent a $(r - R_0)^{-1/2}$ evolution.

3.2. Effect of the injection duration

190 Figure 9 presents the influence on the film spreading of the injection duration T_i for the injection pressure fixed to 100 bar and the distance $z = 50$ mm. T_i is varied from 2 to 12 ms. The two phases (spreading and relaxation) are observed for the 6 different injection durations. Injections for shorter duration have not been performed as it is delicate to visualise the liquid film spreading inside the impingement area. The curves clearly collapse during the spreading phase showing a

195 good control of the injection and the repeatability of the experiments. The final film area is obviously found to increase with the injection time T_i. The relaxation phase seems also to increase with T_i. This point will be analyzed in more details in the following.

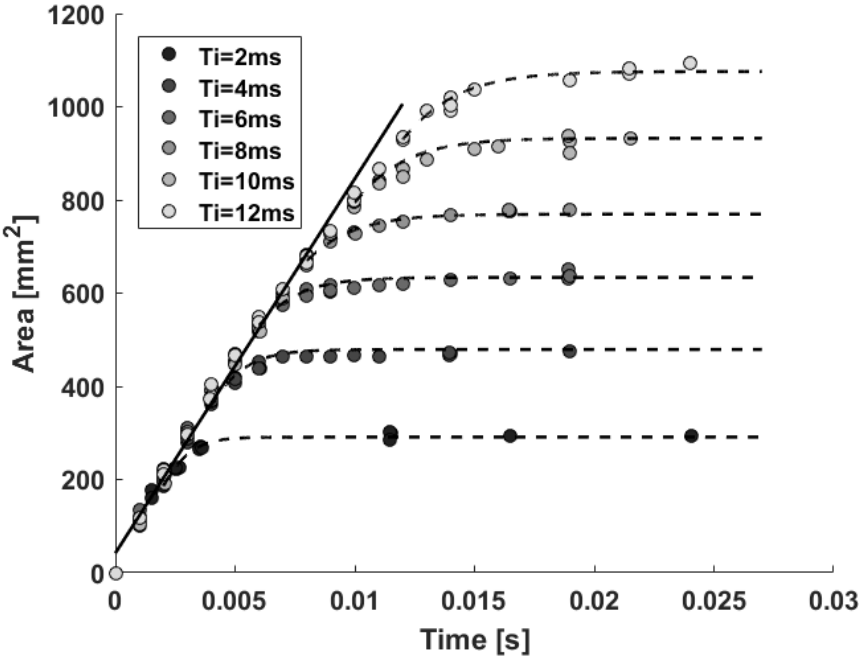

Figure 9: Liquid film area for different injection times. Experimental conditions $P_i = 100$ bar and $z = 50$ mm. Continuous Line: Eq. 8, Dashed line: solution of Eq. 12.

3.3. Effect of the injection pressure

The effect of the injection pressure on the film spreading can be observed in Figure 10. The
200 two distinct phases in the spreading process are confirmed whatever the injection pressure. The spreading rate is clearly depending on the injection pressure. Not only does raising the injection pressure increase the spray momentum, but it also raises the injected mass that has to spread. It is then not surprising that the spreading rate increases with injection pressure, while the global behavior of the film spreading remains the same.

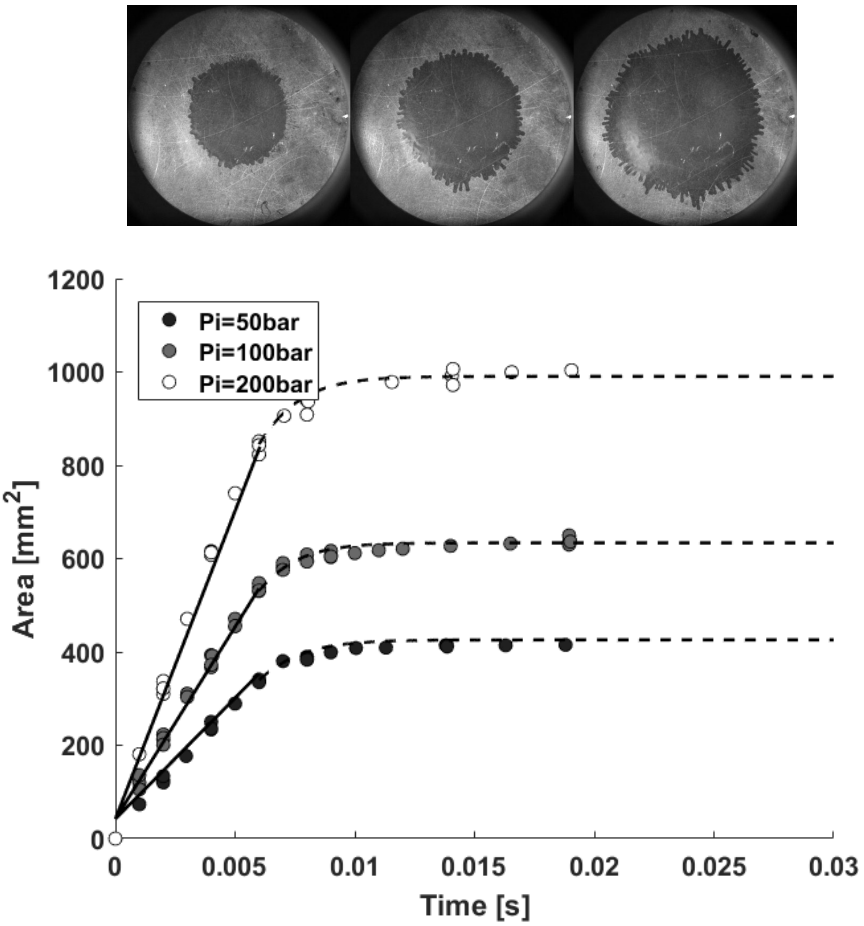

Figure 10: Liquid film area for different injection pressures. Experimental conditions $T_i = 6$ ms, $z = 50$ mm. (top) film at the end of the injection from left to right for P_i=50, 100 and 200 bar. (bottom) Time evolution of the film area. Continuous Line: Eq. 8. Dashed line: solution of Eq. 12.

3.4. Effect of the Injector to wall distance

The injector-wall distance z has been varied from 20 mm to 65 mm. The corresponding effect on the film spreading area is therefore reported in Figure 11 for $P_i = 100$ bar. The same behavior is observed for the three pressure 50, 100 or 200 bar. Film spreading is unchanged when the injector is either closer or further to the impingement plate. This is not a trivial result because, when increasing the distance, the jet is expected to expand and change the impact area on the plate. However for the injector considered here the jet expansion is relatively moderate as illustrated in the image shown in Figure 2. As a consequence the area of impact A_0 is almost constant for the different position z considered. The mean value $A_0 = 42$ mm^2 ($R_0 \approx 3.7$mm) is very close to the value of the mean area of the jet for z between 20 mm to 65 mm. The variation of A_0 with respect to z is small enough to both observe the same behavior and spreading rate as shown in Figure 11.

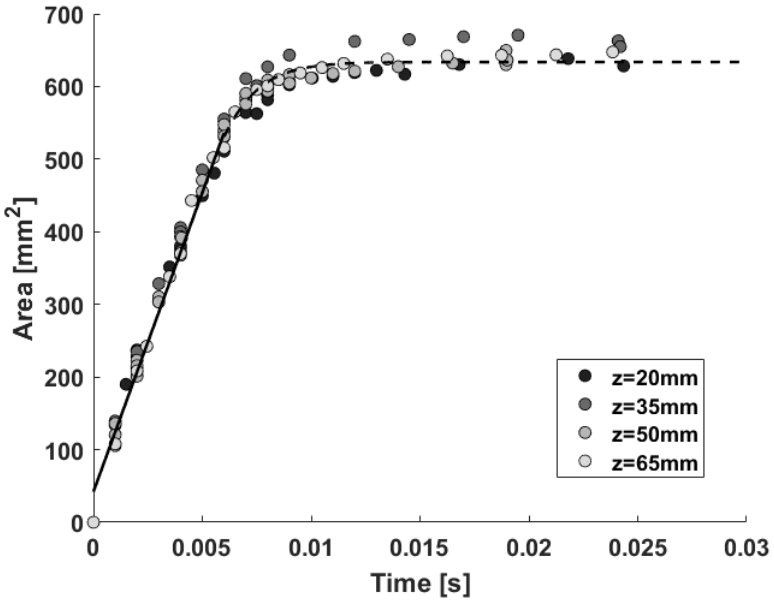

Figure 11: Liquid film area for different injector-wall distances. Experimental conditions $T_i = 6$ ms, $P_i = 100$ bar. Continuous Line: Eq. 8, Dashed line: solution of Eq. 12.

4. The spreading phase

As well underlined in Kalantari and Tropea (2007), spray-wall impingement appears as a very complex phenomenon, with many possible interactions between the incoming droplets and the perturbed film surface. The attention is first drawn to the film propagation, while the injector

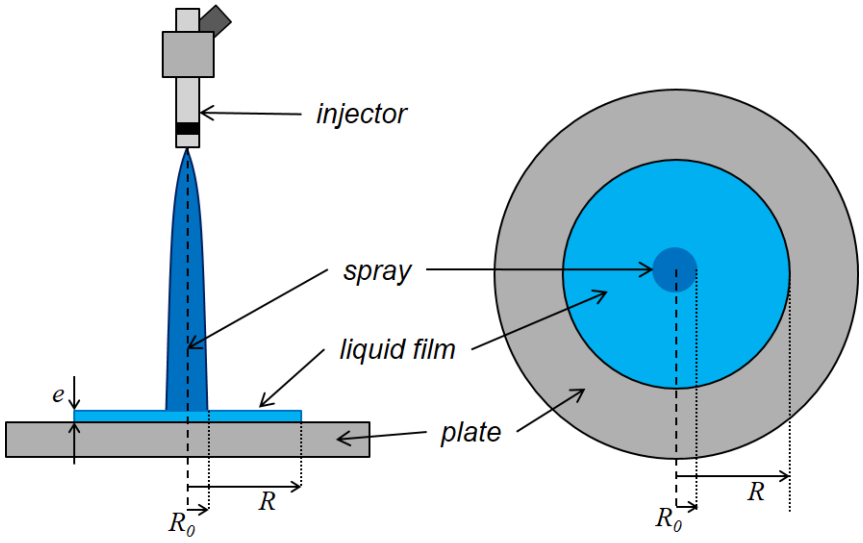

Figure 12: Sketch of the modeled problem. The film thickness is supposed to be homogeneous.

is open. As described above the film spreading from the impact area A_0 is independent on the distance to the wall z while it is controlled by the pressure of the spray at its injection. In the proposed approach, the film shape is simplified to a puddle or a pizza shape, with a uniform thickness e as shown in Figure 12. Mass conservation in the film can then be written as:

$$\frac{d\pi R^2 e}{dt} \approx K_m Q\,, \tag{1}$$

where Q stands for the injection discharge of the injector and K_m represents the injected mass that contributes to the film. $K_m = 1$ corresponds to an injected mass totally transferred into the film. From equation 1, we get the following relation between R and e

$$\pi R^2 e \approx K_m Q t \tag{2}$$

Considering that the pressure gradient induced by the jet impact is balanced by viscous friction, the momentum balance in the film can be simplified to:

$$\frac{\Delta P}{R} \approx \frac{\eta\,\dot{R}}{e^2} \tag{3}$$

because inertia contributions $\rho\ddot{R}$ and $\rho\dot{R}^2/R$ are found to be much smaller than the viscous term and it will be justified latter that the capillary pressure at the liquid front can be neglected compare to the pressure ΔP driving the spreading. The friction at the contact line has also been neglected. Indeed the total friction at the contact line scales as $2\pi R\eta\dot{R}/\theta_d$ times some logarithmic term of order ten (De Gennes, 1985) where θ is the contact line angle. The contact line friction has to be compared to the bulk friction $\pi R^2\eta\dot{R}/e$. The ratio of the two terms scales as $(20/\theta)e/R$ and is of order 0.05 here.

The driving pressure in the film ΔP is governed by the pressure at impact. The relation between the pressure at impact and the pressure of the injector is a delicate question that needs to consider the momentum conservation in the jet. Here, we propose to relate the driving pressure in the film ΔP to the injector pressure P_i through a transfer function K_P such that

$$\Delta P \;\approx\; K_P P_i \tag{4}$$

Substituting in Eq. (3), relation 4 and the value of e expressed from Eq. (2), we get

$$R^5\dot{R} \;\propto\; P_i Q^2 \eta^{-1}\, t^2 \tag{5}$$

Integration of Eq. 5 gives the evolution of the radius with the parameters of the problem as

$$R^2 \;\propto\; P_i^{1/3} Q^{2/3} \eta^{-1/3}\, t\,, \tag{6}$$

showing a linear evolution of the film area in time in agreement with the experimental results presented above. Now substituting Eq. (6) in Eq. (2), we get

$$e \;\propto\; \eta^{1/3} Q^{1/3} P_i^{-1/3}\,. \tag{7}$$

indicating a constant film thickness during the film spreading.

The evolution of the surface area is reported as a function of $P_i^{1/3} Q^{2/3} \eta^{-1/3} t$ in Figure 13 for all the experiments conducted for this study. As shown, all the evolutions are almost collapsing on a single curve showing the relevance of the proposed modeling. As discussed before, the initial area for the film A_0 is almost the same for all the cases and can be related to the mean value of the jet expansion for the distances z considered (from 20mm to 65mm). In particular, equation (6) is able to reproduce the influence of the pressure injection on the film spreading for a large range of pressure. We recover here the same scaling for R as the one observed for the inertial spreading of a droplet deposited on a wall (Winkels et al., 2012; Legendre and Maglio, 2013). However the effects controlling the spreading are different. Indeed, when a single droplet of radius a contacts a solid, the balance between the capillary pressure $\sim a/r^2$ and the inertial pressure $\sim (dr/dt)^2$ gives a base radius evolution of the form $r \sim t^{1/2}$ while here the $R \sim t^{1/2}$ evolution results from the balance between the high pressure driven gradient and the film dissipation (Eq. 3).

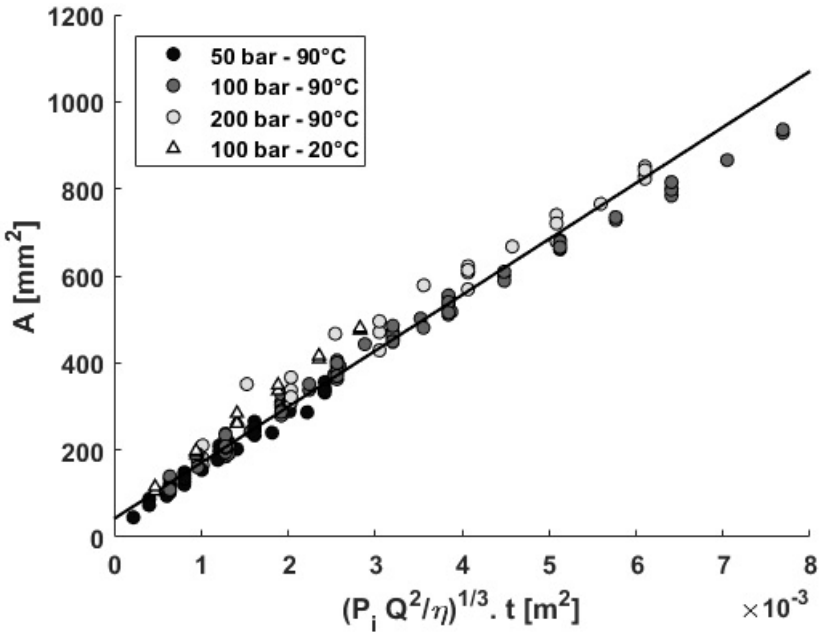

Figure 13: Evolution of the film surface as a function of $P_i^{1/3} Q^{2/3} \eta^{-1/3} t$ for all the experiments conducted for this study. Line: Equation 8 (see the text for the value of K_P and K_m)

A quantitative description of the film area can be provided considering the transfer coefficients K_m and K_P, for the injected mass contributing to the film and for the driving pressure for the film spreading, respectively. The corresponding dependancies of the surface area and the film thickness

are given by

$$\pi R^2 = \pi R_0^2 + \left(\frac{2\pi\, K_m^2\, K_P\, P_i\, Q^2}{\eta}\right)^{1/3} t\,, \tag{8}$$

$$e = \left(\frac{\eta\, K_m\, Q}{2\pi\, K_P\, P_i}\right)^{1/3}, \tag{9}$$

showing that the area of the film formed at the end of the injection is

$$A_i - A_0 = \pi R_i^2 - \pi R_0^2 = \left(\frac{2\pi\, K_m^2\, K_P\, P_i\, Q^2}{\eta}\right)^{1/3} T_i\,. \tag{10}$$

Few studies have been able to determine the mass of liquid injected that effectively contributes to the film under similar conditions of pressure, temperature and mass flow rate. A significant part of the injected mass is either blown out by the air motion induced by the spray impingement (before reaching the plate or after splashing) or vaporized during the travel time of the spray. In Schulz et al. (2016), iso-octane is injected at 150bar in a vessel heated at 80^oC and the injected mass is 21.7mg over 6 holes. The deposited mass for one hole is around 1.4mg which corresponds to a value $K_m = 0.39$. In Ko and Arai (2002), Diesel is injected at 190bar by a one hole injector in non-vaporizing conditions at the distance $z = 50$ mm for single injection. It is found that the mass recovered on the plate is around 50% of the injected mass, and 75% of this mass contributes to the liquid film resulting in the value $K_m = 0.37$. Finally, based on these two studies, the value $K_m = 0.38$ is considered for the following discussion.

The value of K_P is deduced from our experiments considering the evolution reported in Figure 13. From the slope of the general trend, K_P and K_m are connected through the relation $K_m^2 K_p \approx 3.38 \times 10^{-4}$. Considering $K_m = 0.38$ one obtains $K_P = 2.34 \times 10^{-3}$. This value can be discussed considering a simple pressure force conservation in the jet as $\Gamma_{injector} P_i \approx \Gamma_{impact} P_{impact} = \Gamma_{impact} K_p P_i$ where Γ is here the jet cross section. Thus K_p can be roughly related to the jet cross section ratio as $K_p \approx \Gamma_{injector}/\Gamma_{impact} \approx 10^{-3}$, an order of magnitude in agreement with the value $K_P = 2.34 \times 10^{-3}$ deduced from Figure 13. Relation 8 is now reported in Fig. 9, 10 and 11 with $K_P = 2.34 \times 10^{-3}$ and $K_m = 0.38$. As shown, the spreading phase is accurately described for all the experiments. In particular, the effect of the injection pressure is well reproduced (see Fig. 10). Relation 8 is also compared in Fig. 5 with the experiments conducted at the room temperature ($T_{FU} = T_W = 20^o$C) corresponding to a fluid with a larger viscosity. The experimental evolution is recovered with the value $K_m = 0.42$ indicating that a larger amount of liquid contributes to the liquid film when the temperature is decreased because evaporation is reduced in the spray under ambient conditions. With the value of K_p we can now compare the pressure driving the spreading $K_p P_i$ to the Laplace pressure at the film front $\approx \gamma/e$. This ratio is $(\gamma/e)/(K_p P_i) \approx 0.1$ for the minimum pressure $P_i = 50$ bar considered here, showing that capillary effect is not controlling the liquid film spreading.

Having estimated K_P and K_m for the present injection conditions, it is now possible to have an estimation of the film thickness. Considering relation 9, the thickness is $e = 19$, 15 and 12 μm for $P_i = 50$, 100 and 200 bar, respectively. The value of the film thickness, together with the

thickness evolution with respect to injection pressure, are consistent with experiments reported for liquid films under similar injection conditions (Ko and Arai, 2002; Schulz et al., 2016; Schulz and Beyrau, 2018).

The normalized area $A^* = (A - A_0)/(A_i - A_0)$ is finally reported as a function of the normalized time t/T_i in Figure 14 for all the cases considered. The experiments performed for different pressures, temperatures, distances and durations of injection are all collapsing on the $y = x$ line, showing the relevance of the proposed modeling.

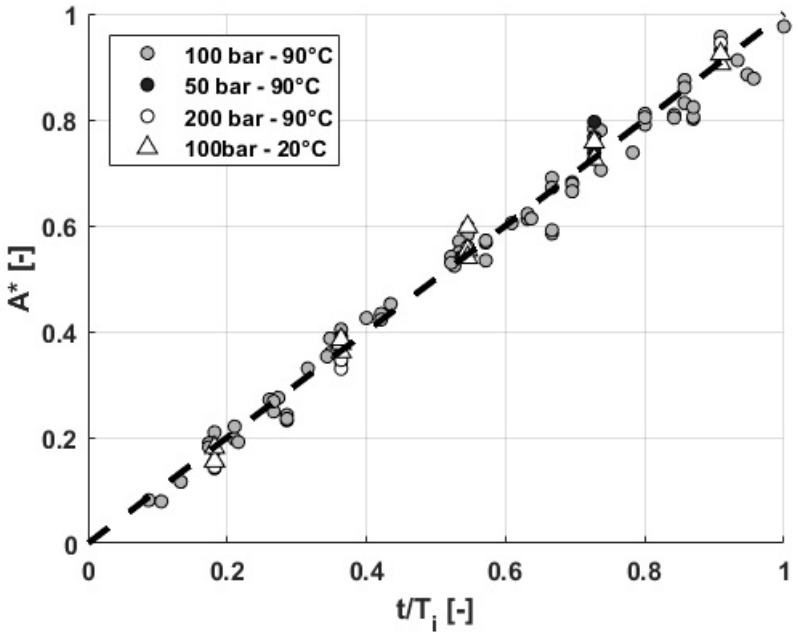

Figure 14: Evolution of the dimensionless area $A^* = (A - A_0)/(A_i - A_0)$ versus the dimensionless time t/T_i for different injection durations and pressures.

5. Relaxation phase

After the end of injection, the liquid film continues to spread even if the source of momentum has been shut down. It has been previously referred as the relaxation phase. The relaxation phase has been observed for all the injection conditions. The radius increase during this phase ranges between 15% to 30%. Once the injection is stopped, the liquid film volume $\Omega_i = \pi R^2 e$ can be considered as constant. During the relaxation, the film momentum is dissipated by viscosity in the film. Considering cylindrical coordinates, the inertial term along the radial direction writes

$$\rho \frac{\partial v_r}{\partial t} + \rho v_r \frac{\partial v_r}{\partial r} \approx \rho \ddot{R} + \rho \frac{\dot{R}^2}{R}$$

Comparing the second term to the viscous contribution $\eta \dot{R}/e^2$ we get from values reported in table 1 $(\rho \dot{R}^2/R)/(\eta \dot{R}/e^2) = \rho \dot{R} e^2/\eta R \approx 0.002$. Thus, only the term $\rho \ddot{R}$ is able to balance the

dissipation in the film so that the momentum equation satisfied in the film writes

$$\ddot{R} \sim -\frac{\nu}{e^2}\dot{R} \tag{11}$$

where $\nu = \eta/\rho$ is the kinematic viscosity. From Eq. 11, the characteristic time of the relaxation phase is then $\tau = e^2/\nu$. Considering the order of magnitude of the film thickness (15μm), we get $\tau \approx 0.4$ ms in agreement with the relaxation phase observed in the above figures. Substituting in Eq. (11) the value of e expressed from the mass conservation $\Omega_i = \pi R^2 e$, one gets the following equation for the film radius during the relaxation phase:

$$\ddot{R} = -C\frac{\nu \dot{R} R^4}{\Omega_i^2} \tag{12}$$

where C is a parameter that a priori needs to be adjusted for the different conditions of injection. Considering the initial values of the film radius R_i and velocity $\dot{R}_i$ for the relaxation phase as the values of R and $\dot{R}$ at the end of injection ($t = T_i$), this equation can be solved to obtain the film radius evolution once the injection is stopped. The corresponding evolutions are reported in Fig. 9 for different injection times and in Fig. 10 for the three pressures of injection considered. As shown in the figures, the relaxation phase is remarkably reproduced by the solution of equation 12. The corresponding values of the parameter C that gets a correct fitting of the experiments are reported in Table 1. The parameter C has the same order of magnitude for all the considered cases, including the experiments conducted at ambient temperature (see Fig. 5, where the solution of equation 12 is reported for $C = 1.78$). C is observed to decrease when increasing the pressure injection.

P_i [bar]	T_i [ms]	R_i [mm]	$\dot{R}_i$[m.s^{-1}]	C [-]
50	6.0	10.4	0.7	2.71
100	2.0	8.0	1.80	2.17
100	4.0	10.7	1.22	2.07
100	6.0	13.0	0.75	1.97
100	8.0	14.9	0.55	1.73
100	10.0	15.9	0.65	1.58
100	12.0	17.8	0.59	1.48
200	6.0	16.4	0.81	1.23

Table 1: Value of the parameter C for different pressures of injection and injection durations.

6. Conclusion

In this paper we studied the spreading process of a liquid film generated by a high-pressure spray on a flat plate. The impingement is made orthogonally to the plate. The experimental set-up allows to follow the edge of the liquid film during the spreading. The conditions of injection,

i.e. pressure, temperature, duration and injector to wall distance have been varied. A detailed inspection of the film spreading has revealed the existence of digitation and surface waves. The film spreading is characterized by two distinct phases. The linear growth of the liquid film area observed during the injection is followed by a relaxation phase that extends the film propagation after the injector needle closing. Both phases have been successfully described using simple modelings based on mass and momentum conservation in the film. The proposed modeling should be extended to consider surface roughness effect. Indeed increasing the roughness will slow down the film progression. Oblique impact, being of great importance for real applications, will be the subject of a following study.

Nomenclature

Roman symbols

A	area of the liquid film,
A_0	area of the impingement area,
A_i	area of the film at the end of injection,
A^*	normalized area of the liquid film
C	parameter used for the relaxation phase
e	liquid film thickness,
K_m	coefficient of deposited mass
K_P	pressure transfer function
$\dot{m}$	mass flow rate of the injector hole,
P_i	fuel injection pressure, bar
ΔP	driving pressure of the liquid film, bar
Q	flow rate of the injector hole,
r	radial coordinate, mm
R	radius of the liquid film, mm
R_0	mean radius of the impingement area, mm
R_i	radius of the film at the end of injection,
$\dot{R}$	speed of the liquid film front
$\ddot{R}$	acceleration of the liquid film front,
t	time,
T_i	duration of injection,
T_{FU}	fuel temperature at injection,
T_W	temperature of the plate,
z	distance between the injector and the plate,

Greek symbols

η	kinematic viscosity of the fuel,
γ	surface tension of the fuel,
Γ	jet cross section,
λ	wavelength of the digitation,

Ω_i liquid film volume during the relaxation phase.
ρ fluid density,
θ_a advancing contact angle,
θ_r receding contact angle,

7. Appendix: High pressurized spray characteristics

In this appendix, we provide the main characteristics of the spray used in our experiments. A description of the injector is first given and then the penetration curve, the spray size distribution and finally the spray angle variation are presented.

7.1. Injector description

The injection system is an experimental 3-hole high-pressure solenoid injector from the automotive industry (gasoline direct injection). It is a high-pressure plain orifice injector as defined and described in Lefebvre and McDonell (2017). The holes diameters measure 165 μm, each one generates a conic spray (Hung et al., 2009), which can be characterized with macroscopic values, such as the tip penetration and the spray angle, and a droplet size distribution (often modeled with a Rosin-Rammler distribution (Lefebvre and McDonell, 2017)). In non-vaporizing conditions, after a few dozens of millimeters, the liquid is fully atomized and the distribution is quite stable and the mean Sauter diameter does not change much, as droplets and air are in a kinematic equilibrium (Sazhin et al., 2003). The Reynolds number at the injector outlet vary between 20,000 and 40,000 for respectively 50 and 200 bar, in the meantime the Weber number vary from 15,000 to 60,000. This corresponds to a fast and fine atomisation process (Lefebvre and McDonell, 2017).

7.2. Penetration curve of the spray

The penetration curve presented here (Figure 15), has been obtained with shadowgraphy. The grey area correspond to the end of the detection frame. The error-bars helps visualise the repeatability of the injection process in term of penetration. The penetration of high pressure sprays is thoroughly studied and many law have been derived in Naber and Siebers (1996); Sazhin et al. (2001); Payri et al. (2011).

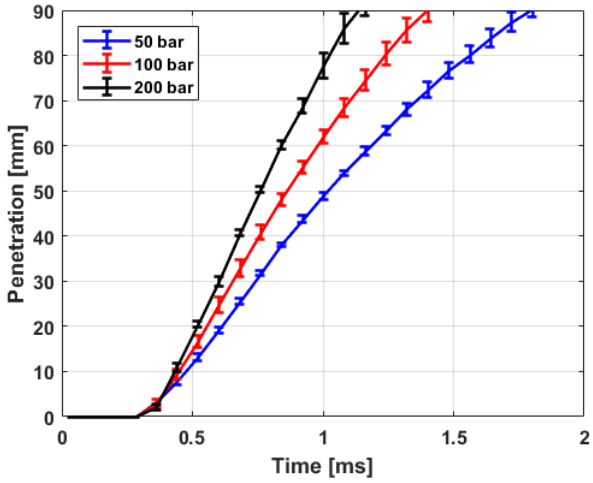

Figure 15: Spray penetration for 50, 100 and 200 bar based on shadowgraphy pictures in atmospheric conditions. Error-bar displaying the standard deviation of measurements based on 5 independent repeats.

7.3. Spray angle

The spray angle is measured using the methodology described in Naber and Siebers (1996). The angle θ of the spray is defined as presented on Figure 16. An isolated jet is relatively narrow, it only slightly varies with injection pressure as indicated by Table 2 resulting in an almost constant area of impact $A_0 \approx 42\text{mm}^2$ with corresponding radius $R_0 \approx 3.7\text{mm}$.

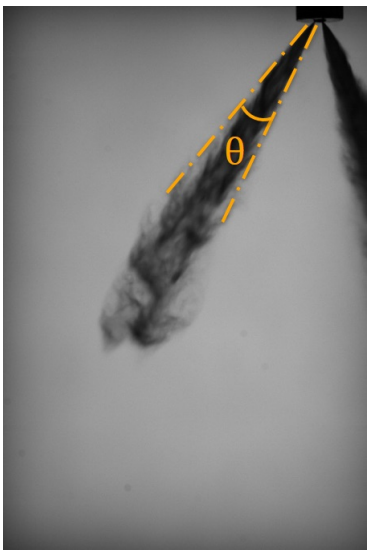

Figure 16: Spray angle definition

7.4. Droplet Size distribution

The spray produced by the injector has been characterized by a spray analyser Spraytec from the Malvern group. An example of spray droplet distribution is reported in Fig. 17 for a pressure

injection of $P_i = 100$bar and a distance to the wall $z = 50$mm. As shown, the distribution can be approximated by a Rosin-Rammler distribution of parameters $X = 18.5\mu m$ and $q = 3$ as defined in Lefebvre and McDonell (2017). The corresponding Sauter mean diameter D_{32} of the spray is given in Table 2. Note that the evolution of the diameter is decreasing with the pressure following a scaling of the form $P_i^{-1/2}$ (Elkotb, 1982).

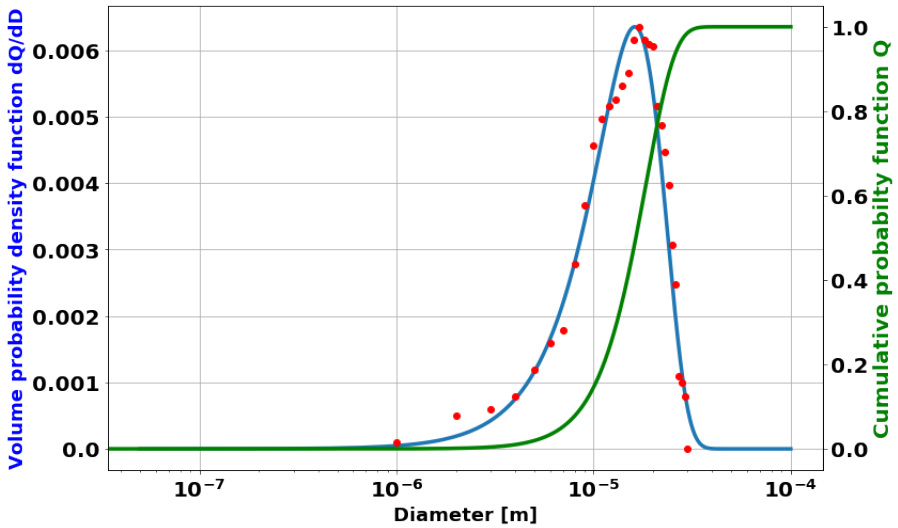

Figure 17: Red: Experimental data of the spray droplet distribution. Blue: Droplet distribution following a Rosin-Rammler distribution of parameters $X = 18.5\mu m$ and $q = 3$. Green: Cumulative probability function.

Pressure [bar]	50	100	200
Spray Angle [^{o}]	9 $\pm 1\mu m$	11 $\pm 1\mu m$	12.5 $\pm 1\mu m$
D_{32} [μm]	14	9.77	7.93

Table 2: Spray angle and Sauter mean diameter D_{32} for the injection pressure considered in this study.

References

References

Araneo, L., Tropea, C., 2000. Improving phase doppler measurements in a diesel spray. SAE Technical Paper .

Ashgriz, N., 2011. Handbook of atomization and sprays: theory and applications. Springer Science & Business Media.

Bonn, D., Eggers, J., Indekeu, J., Meunier, J., Rolley, E., 2009a. Wetting and spreading. Reviews of modern physics 81, 739.

Bonn, D., Eggers, J., Indekeu, J., Meunier, J., Rolley, J., 2009b. Wetting and spreading. Rev. Mod. Phys 81, 739.

Chen, S.J., Tseng, A.A., 1992. Spray and jet cooling in steel rolling. International Journal of Heat and Fluid Flow 13, 358–369.

De Gennes, P.G., 1985. Wetting: statics and dynamics. Reviews of modern physics 57, 827.
Drake, M.C., Fansler, T.D., Solomon, A.S., Szekely Jr, G., 2003. Piston fuel films as a source of smoke and hydrocarbon emissions from a wall-controlled spark-ignited direct-injection engine. SAE transactions , 762–783.
Elkotb, M., 1982. Fuel atomization for spray modelling. Progress in Energy and Combustion Science 8, 61–91.
Fansler, T.D., Parrish, S.E., 2014. Spray measurement technology: a review. Measurement Science and Technology 26, 012002.
Garbero, M., Vanni, M., Baldi, G., 2002. Cfd modelling of a spray deposition process of paint, in: Macromolecular Symposia, Wiley Online Library. pp. 719–730.
Ghosh, S., Hunt, J.C.R., 1994. Induced air velocity within droplet driven sprays. Proceedings of the Royal Society of London. Series A: Mathematical and Physical Sciences 444, 105–127.
Heinlein, J., Fritsching, U., 2006. Droplet clustering in sprays. Experiments in fluids 40, 464–472.
Hélie, J., Khan, M.M., Gorokhovski, M., 2016. Large eddy simulation of a turbulent spray jet generated by high-pressure injection: impact of the in-nozzle flow. Journal of Turbulence 17, 823–846.
Hung, D.L., Harrington, D.L., Gandhi, A.H., Markle, L.E., Parrish, S.E., Shakal, J.S., Sayar, H., Cummings, S.D., Kramer, J.L., 2009. Gasoline fuel injector spray measurement and characterization–a new sae j2715 recommended practice. SAE International Journal of Fuels and Lubricants 1, 534–548.
Huppert, H.E., 1982. Flow and instability of a viscous current down a slope. Nature 300, 427.
Josserand, C., Thoroddsen, S.T., 2016. Drop impact on a solid surface. Annu. Rev. Fluid Mech. 48, 365?391.
Kalantari, D., Tropea, C., 2007. Spray impact onto flat and rigid walls: Empirical characterization and modelling. International Journal of Multiphase Flow 33, 525–544.
Ko, K., Arai, M., 2002. Diesel spray impinging on a flat wall, part i: Characteristics of adhered fuel film in an impingement diesel spray. Atomization and Sprays 12.
Krämer, M., Kull, E., Heldmann, M., Wensing, M., 2014. Investigations on gasoline spray propagation behaviour characteristic for multihole injectors. SAE Technical Paper .
Lamiel, Q., Lamarque, N., Hélie, J., Legendre, D., 2017. Spreading model for wall films generated by high-pressure sprays, in: ILASS-Europe 2017.
Lavalle, G., Sebilleau, J., Legendre, D., 2020. Rivulet cascade from falling liquid films with side contact lines. PHYSICAL REVIEW FLUIDS 5, 124001.
Leach, F., Knorscg, T., Laidig, C., Wiese, W., 2018. A review of the requirements for injection systems and the effects of fuel quality on particulate emissions from gdi engines. SAE Technical Paper 2018-01-1710 .
Lefebvre, A., 1988. Atomization and sprays. CRC press, Taylor & Francis Group.
Lefebvre, A.H., McDonell, V.G., 2017. Atomization and sprays. CRC press.
Legendre, D., Maglio, M., 2013. Numerical simulation of spreading drops. Colloids and Surfaces A: Physicochemical and Engineering Aspects 432, 29–37.
Li, X., Pan, H., Dong, X., Hung, D., Xu, M., 2019. Spray impingement wall film breakup by wave entrainment. Proceedings of the Combustion Institute 37, 3287–3294.
Lighthill, J., 2001. Waves in fluids. Cambridge University Press.
Maligne, D., Bruneaux, G., 2011. Time-resolved fuel film thickness measurement for direct injection si engines using refractive index matching. SAE Technical Paper .
Mohan, B., Du, J., Sim, J., Roberts, W.L., 2018. Hydraulic characterization of high-pressure gasoline multi-hole injector. Flow Measurement and Instrumentation 64, 133–141.
Mojtabi, M., Wigley, G., Hélie, J., 2014. The effect of flash boiling on the atomization performance of gasoline direct injection multistream injectors. Atomization and Sprays 24.
Montanaro, A., Allocca, L., Costa, M., Sorge, U., 2016. Assessment of a 3D CFD model for GDI spray impact against wall through experiments based on different optical techniques. International Journal of Multiphase Flow 84, 204–216.
Moreira, A., Moita, A., Panao, M., 2010. Advances and challenges in explaining fuel spray impingement: How much of single droplet impact research is useful? Progress in energy and combustion science 36, 554–580.
Naber, J.D., Siebers, D.L., 1996. Effects of gas density and vaporization on penetration and dispersion of diesel sprays. SAE transactions , 82–111.
Parrish, S.E., 2014. Evaluation of liquid and vapor penetration of sprays from a multi-hole gasoline fuel injector

operating under engine-like conditions. SAE International Journal of Engines 7, 1017–1033.

Payri, R., Salvador, F., Gimeno, J., Novella, R., 2011. Flow regime effects on non-cavitating injection nozzles over spray behavior. International Journal of Heat and Fluid Flow 32, 273–284.

Sazhin, S., Crua, C., Kennaird, D., Heikal, M., 2003. The initial stage of fuel spray penetration? Fuel 82, 875–885.

Sazhin, S., Feng, G., Heikal, M., 2001. A model for fuel spray penetration. Fuel 80, 2171–2180.

Schindelin, J., Arganda-Carreras, I., Frise, E., Kaynig, V., Longair, M., Pietzsch, T., Preibisch, S., Rueden, C., Saalfeld, S., Schmid, B., et al., 2012. Fiji: an open-source platform for biological-image analysis. Nature methods 9, 676.

Schulz, F., Beyrau, F., 2018. Systematic investigation of fuel film evaporation. SAE Technical Paper .

Schulz, F., Samenfink, W., Schmidt, J., Beyrau, F., 2016. Systematic LIF fuel wall film investigation. Fuel 172, 284–292.

Silvi, N., Dussan V, E., 1985. The rewetting of an inclined solid surface by a liquid. The Physics of fluids 28, 5–7.

Spaid, M., Homsy, G., 1996. Stability of newtonian and viscoelastic dynamic contact lines. Phys. Fluids 8, 460.

Squires, K.D., Eaton, J.K., 1991. Preferential concentration of particles by turbulence. Physics of Fluids A: Fluid Dynamics 3, 1169–1178.

Stevenin, C., Tomas, S., Vallet, A., Amielh, M., Anselmet, F., 2016. Flow characteristics of a large-size pressure-atomized spray using dtv. International Journal of Multiphase Flow 84, 264–278.

Takeda, T., 2006. Study on droplet measurement of unsteady diesel spray using phase doppler anemometry (PDA). Proceedings of ICLASS-2006 233.

Wigley, G., Hargrave, G.K., Heath, J., 1999. A high power, high resolution LDA/PDA system applied to gasoline direct injection sprays. Particle & Particle Systems Characterization: Measurement and Description of Particle Properties and Behavior in Powders and Other Disperse Systems 16, 11–19.

Winkels, K., Weijs, J., Eddi, A., Snoeijer, J., 2012. Initial spreading of low-viscosity drops on partially wetting surfaces. Physical Review E 85, 055301(R).

Xiao, D., Yukihiko, I., Li, X., Hung, D., Nishida, K., Xu, M., 2020. Film breakup of tilted impinging spray under various pressure conditions. International Journal of Engine Research 21, 330–339.

Yang, B., Ghandhi, J., 2007. Measurement of diesel spray impingement and fuel film characteristics using refractive index matching method. SAE Technical Paper .